European Polymer Journal 214 (2024) 113181

Contents lists available at ScienceDirect

European Polymer Journal

journal homepage: www.elsevier.com/locate/europolj

Viscoelastic property enhancement of polymethylmethacrylate molecularly confined within 3D nanostructures

J. Martín-de León [a,c,*], J.L. Pura [b], M.L. Rodríguez-Méndez [b,c], M.A. Rodríguez-Pérez [a,c]

[a] Cellular Materials Laboratory (CellMat), Condensed Matter Physics Department, University of Valladolid, Valladolid 47011, Spain
[b] UVASENS, Escuela de Ingenierías Industriales, Universidad de Valladolid, Paseo del Cauce, 59, Valladolid 47011, Spain
[c] BioEcoUVA Research Institute on Bioeconomy, University of Valladolid, Spain

ARTICLE INFO

Keywords:
Three-dimensional polymer confinement
Amplitude modulation–frequency modulation atomic force microscopy
Nanocellular polymer
Mechanical property
Loss tangent
Confined polymethylmethacrylate

ABSTRACT

Owing to its applications in various fields, such as biomedical, microelectronics, sensors, and polymer composites, polymer nanoconfinement is a widely studied topic. This confinement changes the configuration of molecules compared with those of solids, which, in the case of polymeric films, decreases the glass transition temperature and mechanical properties of the polymer. In this study, nanostructured polymethylmethacrylate, presenting three-dimensional nanoscale confinement were evaluated using amplitude modulation–frequency modulation atomic force microscopy for the first time. The Young's moduli and loss tangents were measured, and the results suggest that for cells smaller than approximately 39 nm, the Young's modulus of the 3-D confined polymer enhances that of the raw solid owing to reduced molecular mobility. This research shows that the molecular mobility was reduced because polymer chains were confined within three-dimensional space.

1. Introduction

1.1. Confinement in polymers

Polymer nanoconfinement has been widely studied because of not only the inherent fundamental science associated with this phenomenon but also the technological implications arising from the use of ultrathin polymeric films in various applications. Such structures are used in biomedical applications, including tissue engineering, wound dressings, and biological membranes [1], and fields, such as microelectronics, sensors, and polymeric composites [2–5].

Polymer nanoconfinement induces molecular changes by altering the molecular mobility and dynamics, interchain entanglements, and even the way stress is transferred between chains compared with those in the same polymer in its bulk state [6]. Such changes strongly affect polymer film macroscopic properties, such as the glass transition temperature (T_g) and mechanical properties [1,7,8]. Therefore, the understanding and control of this confinement is key from a scientific and technological perspective.

In the last few years, considerable effort has been made to study changes in the glass transition temperature (T_g) and relate them to changes in the molecular dynamics of nanoconfined polymers. The magnitude of these changes has been both experimentally measured and theoretically modeled for thin films [9]. Multiple studies have shown that T_g is affected by several variables. For instance, T_g depends on the presence or absence of a substrate or the interaction between the polymer and substrate [10]. Additionally, for some ultrathin films, T_g increases when the thickness reduces in the presence of a specific substrate exhibiting a strong attractive polymer–substrate interaction [11]. However, T_g usually decreases when the film thickness is reduced, which has always been true for freestanding films [8,12–15].

The mechanical properties of such confined structures, on the other hand, have also been investigated. For example, Stafford et al. used buckling-based metrology to measure the elastic moduli of polystyrene (PS), polymethylmethacrylate (PMMA), and polydimethylsiloxane (PDMS) films ranging from 5 to 200 nm thick and found that when the thickness decreased, the elastic modulus drastically decreased, especially compared with that of the bulk [15]. Yiu et al. used dynamic mechanical analysis to measure the stress–strain curves of freestanding PS and PS–PDMS films ranging from 8 to 130 nm thick and found that the Young's modulus decreased with decreasing film thickness, especially at low strain rates [16]. Moreover, PS thin films have shown the same trend using thermal stress techniques, surface wrinkling, and molecular dynamics simulations [17–20]. However, some studies using

* Corresponding author.
E-mail address: judit.martin.leon@uva.es (J. Martín-de León).

https://doi.org/10.1016/j.eurpolymj.2024.113181
Received 4 January 2024; Received in revised form 14 May 2024; Accepted 27 May 2024
Available online 28 May 2024

nanoindentation and bubble inflation rheometry to measure thin films have revealed that mechanical properties improved with decreasing the film thickness [13,21,22]. For nanoindentations, the enhanced mechanical properties have been attributed to the contact stress generated at the probe–polymer interface and the interaction with a much harder substrate and not to the film itself [23]. For bubble inflation rheometry, on the other hand, the origin of the enhanced mechanical properties remains unclear and has been attributed to the measurement heterogeneity. Therefore, previous studies have shown that T_g and mechanical properties usually both decrease when polymer are nanoconfined in the form of a film.

Although some works relate changes in T_g of films to changes in molecular dynamics, multiple works have proven that this is only true for the bulk polymer but in films measurements regarding T_g and molecular mobility are decoupled [24]. However, it seems that in the case of mechanical properties changes can be related to changes in molecular dynamics. A previous study has shown that, unlike polymer chains in bulk materials, those within films are not spherically symmetric but are stretched in the plane and exhibit fewer intermolecular interactions [25]. Additionally, near the material surface, polymeric chains are less intertangled than they are in the bulk, which increases their mobility near free surfaces [26,27]. Thus, as the polymer film thickness decreases, more polymer chains lie on the free surface, which increases the chain mobility of the entire structure and decreases the mechanical properties which is undesirable in many of the previously mentioned applications.

The determination of the mechanical properties of nanoconfined polymers, on the other hand, is not easy. For this objective, atomic force microscopy (AFM) has evolved remarkably during the last decade. One of the most extended techniques for measuring the mechanical properties of nanoconfined polymers is nanoindentation, which enables polymer elastic moduli to be measured fully with nanometric resolution. However, this technique exhibits strong tip–sample interactions, which hinders the isolation of the sample information [23]. Although dual alternating current (AC) resonance tracking (DART) exploits both cantilever flexural modes to enable measurements to be made in the tapping mode [28], the amplitude modulation in both modes does not enable AFM measured quantities (e.g., amplitudes and phases) to be linked directly to material viscoelastic properties, including the Young's modulus. The introduction of amplitude modulation–frequency modulation atomic force microscopy (AM–FM AFM) enables material information about dissipation and complex Young's moduli to be measured directly and rapidly. To the best of our knowledge, AM–FM AFM has only been previously applied to measure viscoelastic properties of bulk polymers, polymer blends, and soft matter in studies by Garcia et al. [29–31]. To date, the application of AM–FM AFM to nanoconfined polymers, especially those in 3D nanoporous structures, remains unexplored, and it is described along this study.

1.2. Nanocellular polymers

In this study, three-dimensional (3D) porous structures (nanocellular polymers) were produced, and their mechanical properties were measured at the nanoscale using AM–FM AFM.

Cellular polymers are biphasic materials comprising a gaseous phase dispersed in a continuous polymeric matrix. When the gaseous phase, i.e., pores or cells, is at the nanoscale, cellular polymers are classified as nanocellular polymers (Fig. 1) [32,33]. As shown in Fig. 1b and c, cell sizes in the nanometric range imply that the solid phase is also within the nanometric scale. Polymeric chains are organized inside cell walls of a certain area and thickness (ξ) much smaller than the cell size (ϕ) (Fig. 1e and f). Cellular polymers can be understood as an entire set of self-standing films placed in a 3D structure, wherein the film area is the surface area of the cell wall (Fig. 1d) and the film thickness is the cell wall thickness (Fig. 1e). The characteristics of the nanocellular materials used in this study are described in the Results section.

The results of this study show that the confinement of the polymer within the 3D nanoporous structure increases the Young's modulus of the solid compared with that of the solid polymer used to produce the nanocellular material and reduces the loss tangent because of hindering of the molecular mobility.

2. Results

2.1. Nanocellular materials

In this study, polymethylmethacrylate (PMMA)-based nanocellular materials were used. As-supplied PMMA pellets were compression-molded to produce 4 mm thick solid sheets (see the details in the Materials and Methods section), which were then used to produce cellular materials through gas-dissolution foaming. Herein, "solid phase" and "solid PMMA" refer to the polymeric phase in the cellular material and "raw polymer" and "bulk PMMA" refer to the PMMA before the cellular

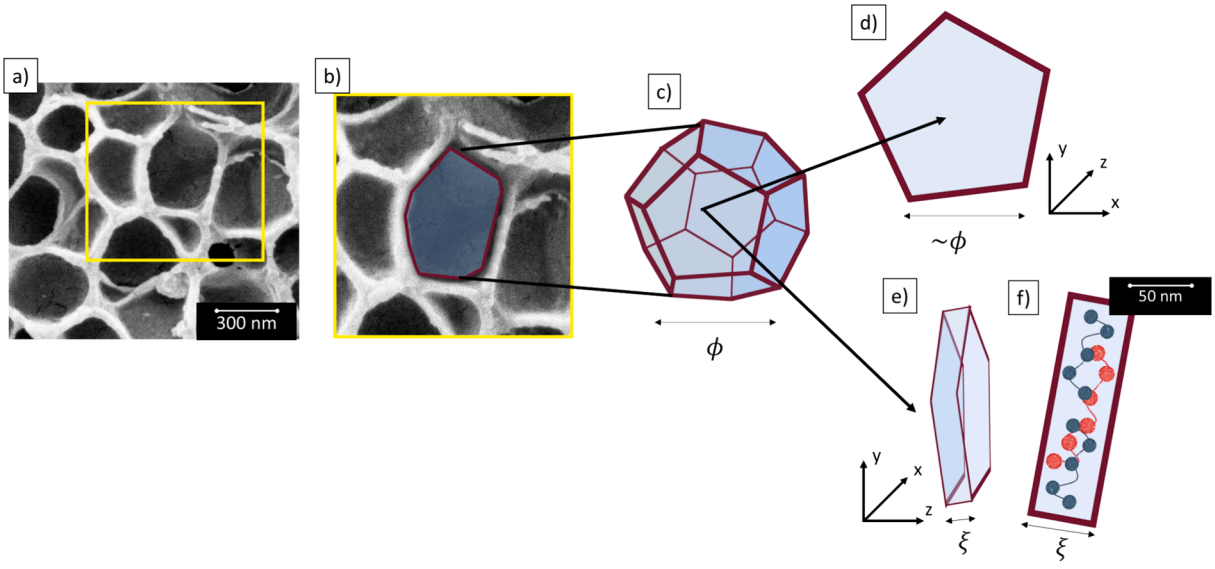

Fig. 1. a) Scanning electron microscopy (SEM) image of nanocellular polymer. **b)** Magnified structural image of single cell. **c)** Schematic of single 3D tetrakaidecahedral cell. Schematics showing **d)** *x*–*y* and **e)** *z*–*y* planes of cell wall and **f)** cell wall of nanocellular material comprising internal polymer chains.

structure was produced.

The properties of the cellular materials used in this study are presented in Table 1. A set of cellular materials exhibiting similar cell sizes (approximately 200 nm) and different relative densities ranging from 0.47 to 0.26 was selected ("A" samples). A second set of cellular materials exhibiting different cell sizes ranging from 217 to 14 nm was used ("B" samples). The relative density (ρ_r), cell size (ϕ), standard deviation of the cell size (SD), cell nucleation density (N_0), theoretical cell-wall thickness (ξ) and open cell content (OC) of the materials are also listed in Table 1. The material characteristics were measured as indicated in the Materials and Methods section.

"A" samples were produced using gas-dissolution foaming with saturation parameters of 31 MPa and 24 °C and foaming temperatures and times ranging from 40 °C to 110 °C and between 1 and 5 min, respectively. A detailed description of the production method can be found elsewhere in the literature [34].

"B" samples were produced using different process parameters. B1 is the mean values of the A-samples. B2 was produced using cyclic gas-dissolution foaming, wherein the saturation conditions of the first and second cycles were 20 and 31 MPa and −32 °C and 24 °C and foaming was conducted at 60 °C and 80 °C for 1 min, respectively. All the sample preparation details are described in a previous study [35]. Finally, samples B3–B5 were produced using saturation pressures of 6, 10, and 20 MPa, respectively, a saturation temperature of −32 °C, and a foaming temperature and time of 60 °C and 1 min, respectively. The production method is described in detail elsewhere in the literature [36].

For the A samples, the relative density changed the most markedly while the cell size remained almost constant. For the B samples, on the other hand, the cell size changed the most remarkably. The effects of these changes on the other cellular material parameters is important for this study. For the A materials, the reduced relative density clearly increases the OC content as ρ_r decreases. For the B materials, the reduced cell size increases the cell nucleation density and decreases the cell-wall thickness. Thus, cell sizes around 200 nm present N_0 around $10^{14} nuclei/cm^3$ and cell wall thickness between 60–100 nm and cell sizes around 14 nm led to $10^{16} nuclei/cm^3$ and 7 nm cell wall thicknesses. This evolution of the cell wall thickness with the reduction of cell size is also appreciable to a lesser extent for A-samples, and it will be really important to understand the mechanical response of the studied samples.

2.2. AM–FM measurements

AM–FM, with a resolution of at least 10 nm, was used to image the samples (Fig. 2b and e) and calculate the loss tangent and measure the Young's modulus locally (Fig. 2c and f) (see the details in the Materials and Methods section).

In addition to the AFM image, the loss tangent ($\tan\delta$) was obtained using the conventional AFM tapping mode for each sample. Because the loss tangent is the dissipated-to-stored power ratio, it is affected by other forces and dissipative processes involved in the tip–sample interaction. Therefore, obtained loss tangents represent an upper bound for the actual material loss tangent.

The Young's modulus, on the other hand, was measured using the AM–FM mode by relying on the use of two tip resonant modes simultaneously. For each sample, the Young's modulus was obtained by assuming a Hertz punch model interaction [29], and the Young's modulus of raw PMMA (3.7 GPa) was used as a reference (see the Materials and Methods section for additional details).

Three images per sample, at different length scale, were obtained at 3×3, 1.5×1.5, and 0.5×0.5 μm^2. The maximum and mean Young's moduli and mean loss tangent were extracted from each image, taking particular attention to possible experimental artifacts. Finally, the obtained values were divided by corresponding values for raw PMMA to obtain the specific Young's modulus (E_r) and specific maximum Young's modulus ($E_{r_{max}}$).

2.3. Young's moduli for solid phase at scale of hundreds of nanometers: Influence of density on Young's modulus

The A samples were selected to study the mechanical response of the solid phase within a porous structure comprising approximately 200 nm cells and cell-wall thicknesses ranging from 60 to 100 nm. The influence of the relative density on the Young's modulus can be studied for these samples. In particular, the A samples present cell sizes between 184 and 234 nm, cell-wall thicknesses from 57 to 120 nm (Table 1), and a range of relative densities from 0.26 to 0.47.

The mean and maximum specific Young's moduli of the solid phase are plotted as functions of the relative density in Fig. 3. The magnitudes of both exhibit a similar behavior, i.e., the lowest-density samples

Table 1
Characteristics of nanocellular materials used in this study [34–36].

Sample	Relative density	Cell size (nm)	SD (nm)	N_0 ($1/cm^3$)	ξ (nm)	OC (%)
A1	0.47	212	95	$1.8 \cdot 10^{14}$	84	4
A2	0.38	207	87	$2.4 \cdot 10^{14}$	68	5
A3	0.37	184	73	$3.1 \cdot 10^{14}$	57	8
A4	0.37	225	87	$2.2 \cdot 10^{14}$	70	8
A5	0.35	221	97	$2.3 \cdot 10^{14}$	65	12
A6	0.29	224	91	$2.8 \cdot 10^{14}$	117	91
A7	0.28	234	100	$2.7 \cdot 10^{14}$	119	100
A8	0.27	222	89	$3.0 \cdot 10^{14}$	113	99
A9	0.26	227	91	$3.2 \cdot 10^{14}$	112	90
B1	0.34	217	90	$2.5 \cdot 10^{14}$	62	65
B2	0.26	100	35	$2.2 \cdot 10^{15}$	22	100
B3	0.56	39	10	$7.7 \cdot 10^{15}$	19	100
B4	0.6	24	6	$1.2 \cdot 10^{16}$	12	100
B5	0.55	14	3	$4.0 \cdot 10^{16}$	7	100

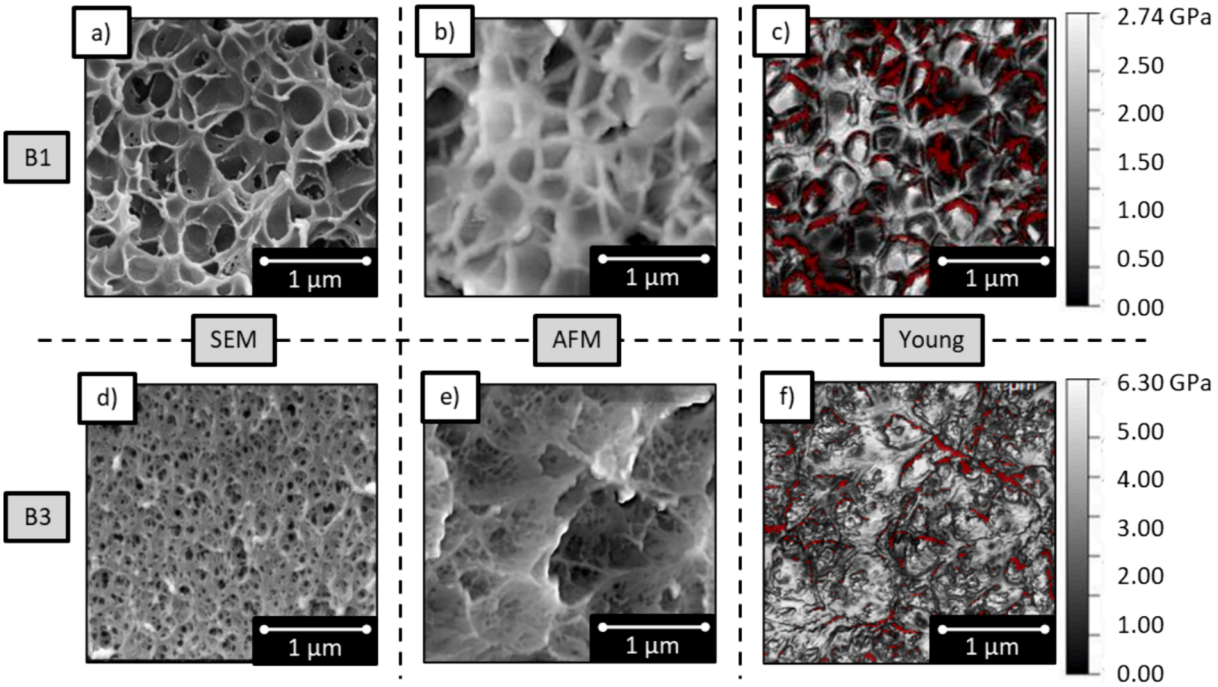

Fig. 2. a, d) Scanning Electron Microscopy (SEM) micrographs; **b, e)** Atomic Force Microscopy (AFM) images; and **c, f)** Young's modulus maps of samples B1 and B3, respectively.

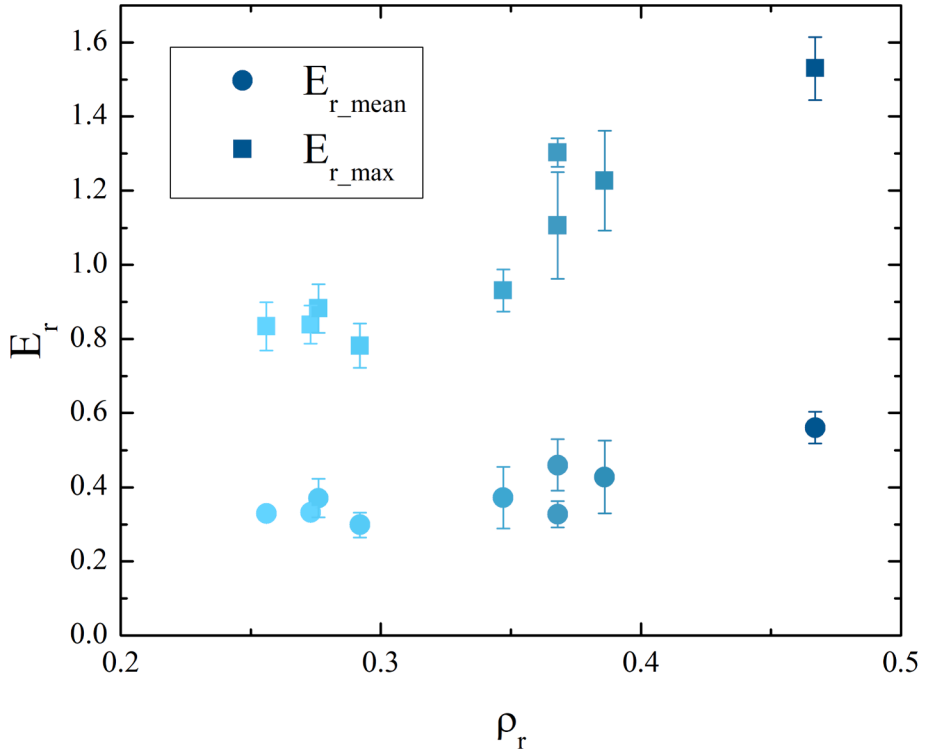

Fig. 3. Mean and maximum specific Young's moduli plotted as functions of relative density.

present very similar Young's moduli. However, with increasing relative density >0.3, the Young's modulus rises. The highest-density samples ($\rho_r > 0.35$) present local maxima higher than those measured for the solid PMMA sheet polymer. However, for all the samples, the mean value is <1, meaning that compared with the raw PMMA, the solid phase in the cellular material presents a reduced E value.

The observed changes in the relative density are triggered by changes in the gas-phase concentration, both the cell size and number (i.e., cell nucleation density) (Table 1). Additionally, such changes in the gaseous phase imply some important structural changes in the solid phase. To elucidate the Young's modulus evolution, the dependence of the Young's modulus was studied for parameters defining both gaseous and solid phase. As shown in Fig. 3, because the $E_{r_{max}}$ trend is more pronounced, the magnitude of $E_{r_{max}}$ was studied.

Fig. 4 shows $E_{r_{max}}$ plotted as functions of the cell size, cell nucleation density, theoretical cell-wall thickness, and OC. In addition, the blue intensity indicates the relative density magnitude; i.e., the darker the color, the higher the density.

Notably, above a threshold value for all the magnitudes, the relative Young's modulus slightly increases. Fig. 4.a shows how samples comprising small cells usually exhibited both the highest density (darkest color) and the best mechanical performance. However, the sample with the smallest cells (A3) still exhibited a high Young's modulus although the relative density is not the highest one and cell nucleation density is relatively low. Although the Young's moduli only slightly changed, the obtained results may indicate that the cell size is an important parameter to consider.

For the solid phase, the dependence of the Young's modulus on both ξ and OC is shown in Fig. 4c and d, respectively. The lowest-density samples exhibited the highest OC and thinnest cell walls. Although the samples presenting a completely open structure exhibited cell walls thicker than 100 nm, the highest-density samples presenting an almost-closed structure exhibited much thinner (up to 60 nm) cell walls (Table 1). The increase in the Young's modulus with the decreasing OC, suggests that thinner cell walls could improve mechanical properties. These changes in the solid phase may affect the molecular configuration and, therefore, mechanical properties of the solid phase. However, because the observed trends are subtle, samples exhibiting much different structures were studied for a much more in-depth analysis.

Therefore, the introduction of the solid phase within approximately 100 nm thick cell walls negligibly changed the Young's modulus compared with those of cellular materials exhibiting thicker cell walls. In addition, the mean mechanical responses were worse than those of corresponding bulk materials.

2.4. Young's moduli for solid phases at scale of tens of nanometers

For the B samples, the Young's modulus 3D maps (Methods section for further details) are shown in Fig. 5.

Clearly, the dynamic range of the Young's modulus color scale changes with decreasing cell size. To obtain 3D maps comprising a similar color range, the scale maximum must be increased from 2.8 to 18 GPa for approximately 200 and 14 nm cells, respectively. To quantify these changes, the maximum and mean specific Young's moduli are plotted as functions of the cell size (Fig. 6).

Obviously, the magnitudes of both suddenly increased with decreasing cell size, suggesting that there exists a cell size threshold below 100 nm for which the Young's modulus of the solid phase increases sharply and considerably surpasses that of bulk polymer. For cells smaller than 50 nm, not only the local Young's moduli are above that of the bulk polymer but also the mean Young's modulus of the solid phase indicates that the polymer within the cellular structure performs better than the bulk. Thus, for the sample comprising 14 nm cells, E is more than three times higher than that of the solid, and the local maximum E values are almost five times higher than the maximum E of the raw polymer.

The reduction of the cell size reduces the cell-wall thickness of the cellular material, meaning that the polymer chains are forced to order within less space as the cells become smaller. According to previously published studies, molecular chains confined within thin films increase the molecular mobility and reduce the Young's modulus [20]. Therefore, to study the molecular mobility within the structure in this study, the loss tangent was measured and is plotted as a function of the cell size in Fig. 7a.

Fig. 7a shows that the reduction of the cell size reduced the loss tangent. As described in section 4.2.4 this measurement was carried out at room temperature. The loss tangent can be associated to some relaxation process or the molecular mobility of polymeric chains. Since

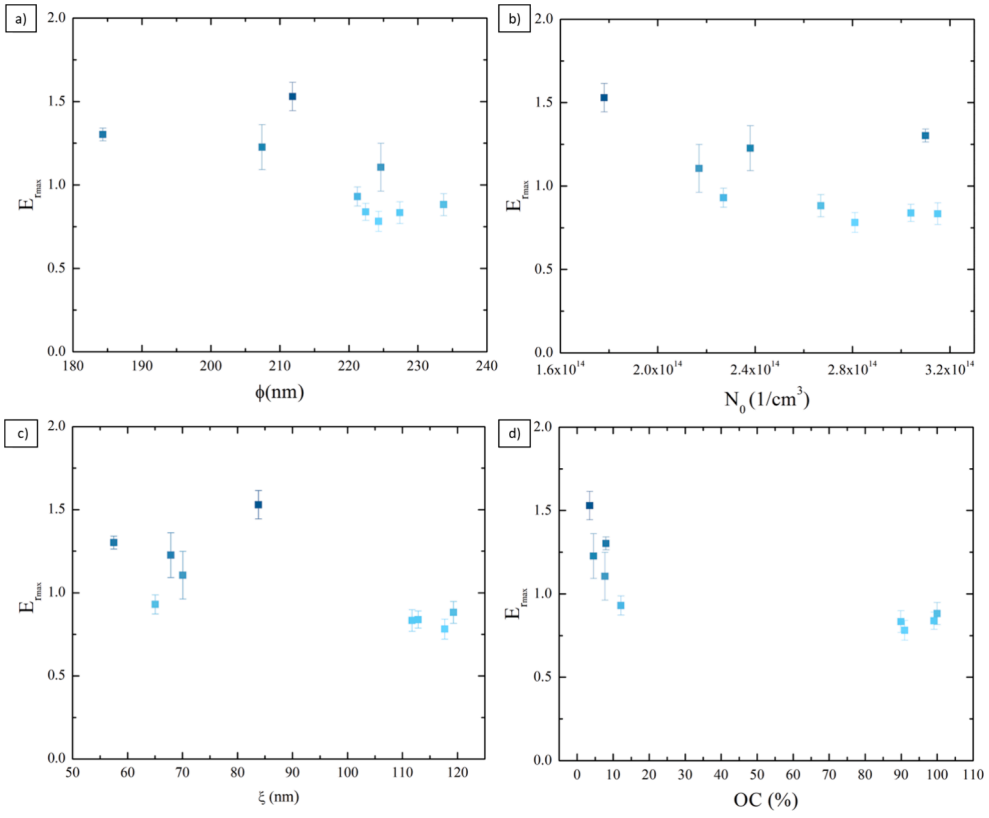

Fig. 4. Maximum specific Young's modulus plotted as functions of **a)** cell size, **b)** cell nucleation density, **c)** cell-wall thickness, and **d)** open cell content. Color intensity indicates magnitude of relative density, wherein darkest color corresponds to highest relative density.

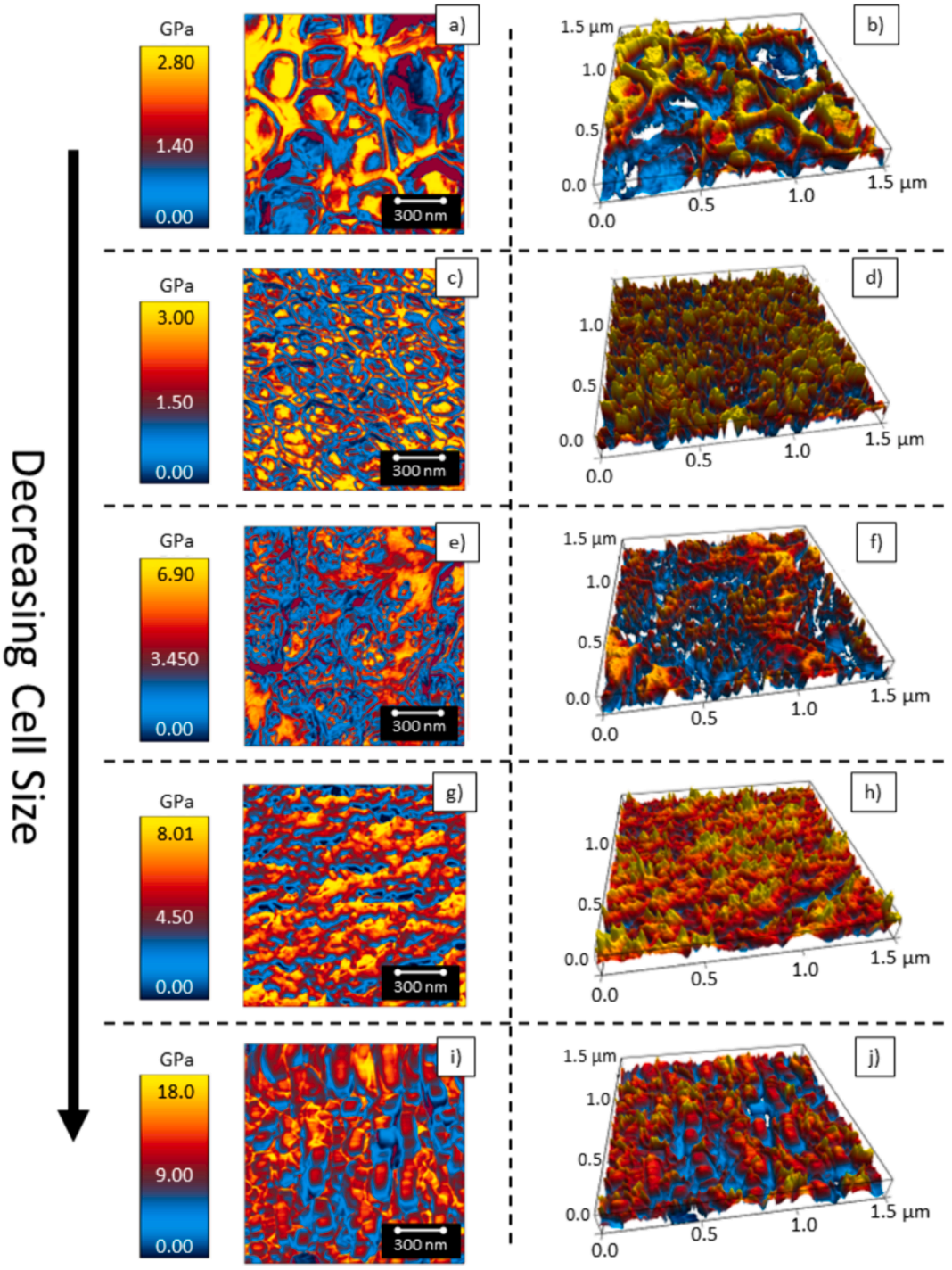

Fig. 5. Cell-size dependence of Young's modulus (3D maps) for B samples comprising **a, b)** 217; **c, d)** 100; **e, f)** 39; **g, h)** 24; and **i, j)** 14 nm cells.

PMMA do not present any relaxation process at room temperature (see Figure S1 in Supporting Information), a higher tanδ is associated to a higher mobility, meaning that in these structures, unlike in 2D films, the reduction of the cell size reduced the molecular mobility. As shown in Fig. 7b, the lower the tangent, the higher the $E_{r_{max}}$ value, suggesting that lower molecular mobilities stiffen the polymer matrix.

In the amorphous bulk, the polymer chain size can be defined by its radius of gyration $\left(R_g = \langle R^2 \rangle^{\frac{1}{2}}\right)$ and end-to-end distance (R) [37]. R_g is the root-mean-square distance of the chain segment from the chain's center of mass, while the end-to-end distance represents the separation between the beginning and end of the polymer chain (Fig. 8a). PMMA presents a wide molecular weight distribution, wherein the mean M_w (=83 kg/mol) indicates the mean weight of the polymer chains and M_{z+1} (=149 kg/mol) indicates the weight of the longest polymer chains. The upper bound for the molecular weight $(M_{\max})$ is 242 kg/mol. The chain length, end-to-end distance, and radius of gyration were calculated using both molecular weights (Table 2). Clearly, in the bulk polymer, the polymer chain presents a mean R value of 20 nm, while the longer chains present a maximum R value ranging from 26 to 33 nm and a mean R_g value of 8 nm, with the longest chains presenting a maximum R_g value ranging from 11 to 13 nm.

For the nanocellular polymers in this study, these molecular chains are forced to arrange within cell walls in three spatial directions. If

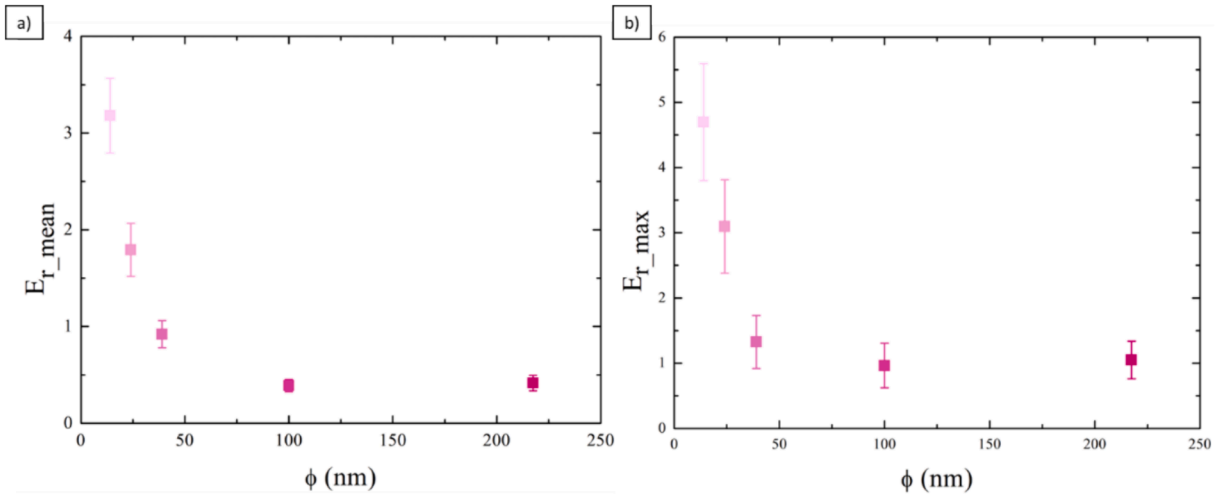

Fig. 6. **a)** Mean and **b)** maximum specific Young's moduli plotted as function of cell size. Color scale indicates different cell sizes.

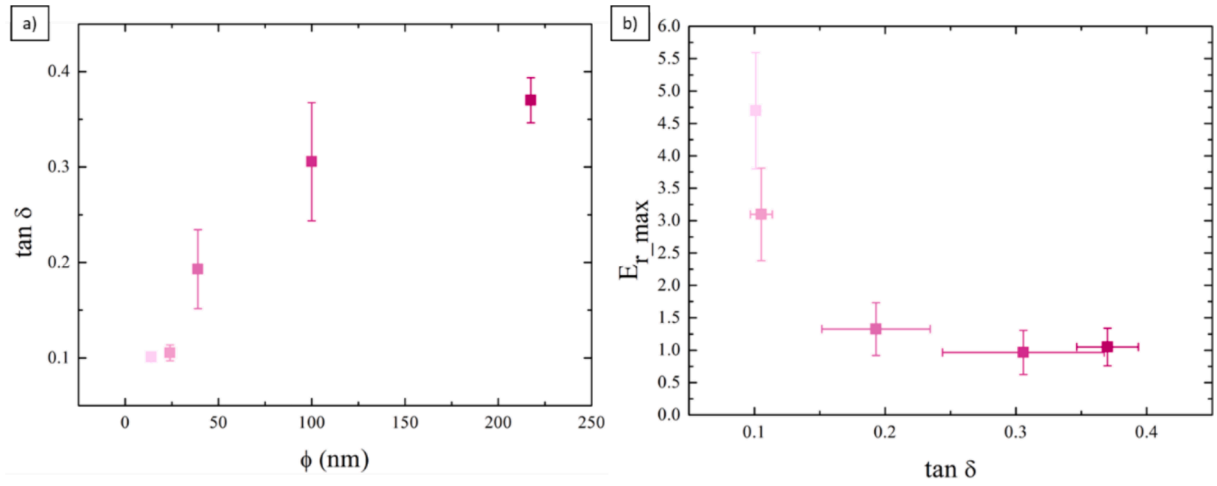

Fig. 7. **a)** Loss tangent plotted as function of cell size. **b)** Maximum specific Young's modulus plotted as function of loss tangent.

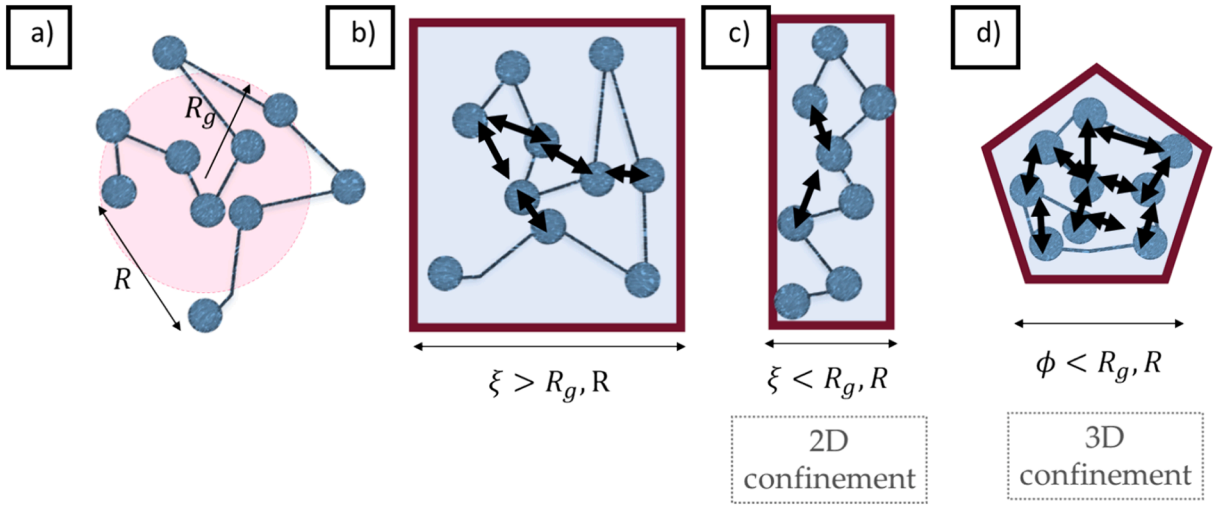

Fig. 8. Schematics showing **a)** radius of gyration and end-to-end distance of polymer chain configured in bulk; polymer chains confined within cell walls **b)** thicker and **c)** thinner than gyration radius, respectively; and **d)** polymer chain confined within 3D nanopore wall smaller than gyration radius.

Table 2
PMMA chain length, end-to-end distance (R), and gyration radius (R_g) calculated using M_w, M_{z+1}, and M_{max}.

	Chain length (nm)	R (nm)	R_g (nm)
M_w	276	19.55	7.98
M_{z+1}	493	26.00	10.61
M_{max}	802	32.98	13.46

considering cell walls as thin films of thickness ξ, when a single cell wall is thick enough (Fig. 8b), the polymer chain will present the same configuration as that in the raw material, meaning it has same molecular interactions. However, if the cell wall is thinner than the polymer chain dimension (Fig. 8c), the configuration will be less folded and exhibit fewer molecular interactions than the one in the solid [27]. This is called "one-dimensional (1D) confinement" and has previously been discussed for thin films. If the film surface area, defined by ϕ^2, on the other hand, is smaller than that of the polymer chain (Fig. 8d), the polymer chain will be confined in all directions, and the final polymer chain configuration will be different from that in the solid, which will lead to higher molecular mobility and more molecular interactions. However, results in this work show that this 3D structure cannot be considered as a collection of isolated 2D films, but a collection of interconnected films that leads to a 3D confined structure. Therefore, the polymer chain will be confined in three spatial directions, which can be defined as 3D confinement. In this case, polymer chains will arrange in a three-dimensional and interconnected structure, and, thus, the molecular disposition will be different from that in a 2D film, never having the polymer near a free surface but 3D confined.

Therefore, for these materials, two magnitudes can be defined as $C_{1D} = \xi/R$ and $C_{3D} = \phi/R$. When these magnitudes are less than unity, the polymer is forced to arrange in a smaller space than that in the solid disposition. To evaluate when the polymer chains start to be confined, these magnitudes were calculated for R_{Mz+1}.

According to the data listed in Table 3, 1D confinement begins for cells smaller than 100 nm, which is enough to increase the polymer T_g, as indicated in previous studies [34], and suggests that in this structure, the 1D confinement is unlike that in films (in which T_g decreases with confinement) owing to the three-dimensional arrangement. However, such 3D porous materials do not still exhibit improved mechanical properties. The evaluation of C_{3D}, on the other hand, reveals how polymeric chains start becoming 3D-confined for materials comprising cells <39 nm, for which the Young's modulus starts improving.

Although film-like structures are produced near equilibrium, nanocellular foams are produced from strong thermodynamical instability, which enables such structures exhibiting extraordinary mechanical properties to be generated far from equilibrium. In addition, the macroscopic mechanical properties of nanocellular polymers have recently been presented in other studies [38,39]. Although some previous studies have shown that above a certain cell size, mechanical properties improve, the mechanism through which this occurs has never been proven. The results of this study indicate that the explanation of this improvement is at a molecular scale and that the improved solid phase could enhance the mechanical properties of the entire cellular material.

Table 3
Characteristics of nanocellular materials used in this study and produced in previous studies and magnitudes defined to evaluate 1D and 3D confinements [34-36].

ϕ(nm)	ξ (nm)	C_{1D}	C_{3D}
225	62	2.38	8.65
100	22	0.85	3.85
39	19	0.73	1.50
24	12	0.46	0.92
14	7	0.27	0.54

Therefore, at the nanoscale, polymer mechanical properties can be improved by confining polymer chains in 3D nanostructures, which can enable the implementation of polymers in applications, wherein such polymers were previously unusable owing to mechanical integrity requirements, and revolutionize fields, such as surgical treatments, microelectronics, polymer nanocomposites, membranes, sensors, and aeronautic and automotive applications.

3. Conclusions

The Young's moduli and loss tangent of nanoporous PMMA were studied using AM–FM AFM.

In nanocellular porous structures, polymeric chains are organized within the solid phase forming the cells. In this study, materials exhibiting cells around 200 nm and relative densities ranging from 0.47 to 0.26 and a set of materials comprising cells ranging from 200 to 14 nm were analyzed. These materials have cell walls with a surface area around the cell size squared, and a thickness ranged from 62 to 7 nm, respectively.

In the sample comprising 200 nm cells, the average Young's modulus of the solid phase was less than that measured for the raw polymer and increased with increasing relative density. Changes in the relative density are related to changes in both the cell size and cell nucleation density, which simultaneously modify the morphology of the solid phase. The samples comprising the smallest cells and exhibiting higher densities lead thinner cell walls and slightly higher mechanical properties.

With decreasing cell size from 200 to 14 nm, on the other hand, the Young's moduli of the solid phase clearly improves for cells smaller than 39 nm. Below this cell size value the Young's modulus was enhanced compared with that of the solid polymer. Moreover, for the material comprising 14 nm cells, the Young's modulus and local Young's moduli were three and more than five times higher than those of the raw polymer, respectively. Compared with the sample comprising 200 nm cells, the sample comprising 14 nm cells exhibited a loss tangent that was four times lower, which suggests that the improved Young's modulus is attributed to the reduced molecular mobility of polymeric chains.

The study of the morphology of the polymer chains within the cellular structure clearly revealed that polymer confinement within one dimension produces chains exhibiting a molecular mobility similar to those chains in the raw polymer. However, the presence of a 3D structure with the three dimensions of the space being smaller than the dimension of the original polymer chains leads to a 3D confinement that increases molecular interaction and reduces molecular mobility and, therefore, considerably increases the polymer mechanical response.

4. Materials and methods

4.1. Materials

4.1.1. Solid PMMA

The raw material, polymethylmethacrylate (PMMA; V825T grade) pellets, was supplied by ALTUGLAS® International (Colombes, France). The PMMA had molecular weights (M_n and M_w) of 43 and 83 kg/mol, respectively, as measured using gel permeation chromatography, a glass transition temperature (T_g) of 114 °C, as measured using differential scanning calorimetry, and a density of 1.19 g/cm^3, as measured at 23 °C and 50 % relative humidity.

The solid PMMA had a melt-flow index of 1.92 g/10 min, as measured at 160 °C/10 kg, a zero-shear viscosity of 7095 Pa•s, as measured using shear rheology, and a Young's modulus of 3.7 GPa, as measured using tensile tests on a universal testing machine INSTRON (model 5.500R6025). Strain/stress curves were obtained following the ISO527 standard at room temperature and a strain rate of 2 mm/min.

4.2. Methods

4.2.1. Compression molding

Solid PMMA sheets (4 mm thick) were produced by compression-molding PMMA pellets. The PMMA pellets were dried overnight at 70 °C and then heated at 200 °C for 9 min. For an additional minute, a pressure of 42 MPa was applied while maintaining the temperature. Finally, the molded PMMA sheets were cooled at the ambient temperature and same pressure.

4.2.2. Density

The density (ρ_s) of the raw PMMA was measured using gas pycnometry (AccuPyc II 1340, Micromeritics, Norcross, GA, USA). The density (ρ_f) of the cellular materials was determined using the Archimedes' principle-based water displacement method and an AT261 Mettler–Toledo balance. The relative density is defined as the cellular-to-raw material density ratio (Eq. (1)) as follows:

$$\rho_r = \frac{\rho_f}{\rho_s} \tag{1}$$

4.2.3. Cellular structure

The cellular structure (Fig. 2a and d) was visualized using field-emission scanning electron microscopy (FESEM; FEI QUANTA 200 FEG, Hillsboro, OR, USA) and a method published in a previous study [36]. Prior to visualization, it is necessary to follow the next procedure. Firstly, samples were fractured after immersion in liquid nitrogen to ensure that the cellular structure was preserved. Then, the surface was coated with a 5–10 nm thick layer of gold or iridium using a sputter coater (model SDC 005, Balzers Union, Balzers, Liechtenstein). The obtained micrographs were analyzed using ImageJ/FIJI-based software to obtain the cell size, standard deviation of the cell size, and cell nucleation density [40]. Each SEM image was masked, which enabled the software to obtain quantitative data for the cellular structure [40]. To validate the data homogeneity, a minimum of 200 cells were analyzed in different regions for each material, which enabled the cell size corresponding to the mean diameter of the measured cells and corresponding standard deviation to be obtained. In addition, the cell nucleation density represents the number of nucleation points per unit of volume of the raw material and was determined using Kumar's method [41].

For nanocellular materials, because the micrograph resolution hinders the experimental measurement of the cell-wall thickness (especially for cells smaller than 100 nm, see Fig. 2d), theoretical approaches can be used instead. In this study, the cells were assumed to exhibit a tetrakaidecahedral geometry, and Eqs. (2) and (3) were used to determine the cell-wall thicknesses (Table 1) of the closed and open cellular materials [42], respectively, as follows:

$$\xi = \frac{\phi\rho_r}{1.18} \tag{2}$$

$$\xi^2 = \frac{\rho_r\phi^2}{1.06} \tag{3}$$

Eqs. (2) and (3) were used for samples A_1–A_5 and the remaining samples, respectively.

4.2.4. AM–FM AFM

AM–FM AFM (Cipher ES Environmental AFM, Oxford Instruments, Asylum Research, Wiesbaden, Germany) was used to analyze the sample surfaces. The Young's moduli were locally measured using the AM–FM viscoelastic mapping mode. The microscope was equipped with an AC160TSA-R3 tip (Oxford Instruments, Asylum Research, Wiesbaden, Germany) and operated in tapping mode with blueDrive photothermal excitation.

Conventional AFM tapping-mode imaging operates by fixing the tip–substrate distance and scanning the sample surface. The cantilever is driven to oscillate in its fundamental flexural mode (at a fixed frequency) to maximize the recorded signal and signal-to-noise ratio. The tip–substrate distance is maintained by a feedback loop that varies the cantilever vertical position (z-axis). During scanning, variations in the cantilever oscillation amplitude and phase are registered to provide information about the surface topography and material loss tangent ($\tan\delta$) at a nanometric resolution. The latter can be calculated using the measured amplitude (A) and phase (φ) and the following relationship (Eq. (4)) [43]:

$$\tan\delta = \frac{\frac{A}{A_0} - \sin\varphi}{\cos\varphi} \tag{4}$$

where A_0 is the free oscillation amplitude (measured far from the sample surface).

4.2.5. Young's modulus measurements

The AM–FM mode relies on the use of two resonant modes of the tip simultaneously: the fundamental mode, which is operated in amplitude modulation, as in the standard AFM tapping mode, and, typically, the second resonant mode (at a higher frequency), which is operated in frequency modulation, hence the name AM–FM. In FM, similar to AM, the second mode phase is constantly maintained at 90° by adjusting the drive frequency in a feedback loop. During scanning, the recorded frequency shifts are proportional to changes in the contact stiffness and sample elastic modulus. Moreover, by constantly maintaining a 90° phase, the FM mode does not perturb the AM fundamental mode, which provides measurement stability and robustness. Notably, both modes are simultaneously excited, which enables the combined acquisition of topography and loss tangent images with the viscoelastic information provided by the FM mode. The elastic modulus can be directly determined from these measurements using contact mechanics models [31,44]. However, the use of a reference sample with a known Young's modulus is much simpler for calibrating system parameters and guarantees that the exact cantilever shape does not affect the final results because of the system linearity. This will be the approach used in this work, raw PMMA was used as a reference for calibrating the system, and the magnitudes measured for the foam directly referred to the analogous magnitudes measured for the solid. By assuming a Hertz punch model interaction, the functional dependence of the Young's modulus can be expressed as follows (Eq. (5)) [29]:

$$E' = \frac{k_2}{r_c}\frac{\Delta f_2}{f_2^0} = C\Delta f_2 \tag{5}$$

where r_c is the tip radius; k_2 and f_2^0 are the spring constant and free oscillation frequency of the cantilever's second resonant mode, respectively; and Δf_2 is the frequency shift recorded in the FM mode. Although the proportionality constants could be different depending on the tip–sample modeling, the relationship between the Young's modulus and frequency shift will always be linear, which is sufficient to calibrate the proportionality constant (C) for any tip. This is conducted by measuring the surface of a raw PMMA sample identical to that used as a precursor for the studied nanocellular foams. The control software of the Cypher AFM allows to apply this model during AFM operation and directly provides the Young's modulus and loss tangent images, together with the other images simultaneously obtained: amplitude, phase, frequency shift, etc. In the selected calibration model, the tip radius is the free parameter, which is adjusted until the average Young's modulus of the reference sample is 3.7 GPa and is maintained for all the measurements until the tip shows evidence of wearing or is changed.

CRediT authorship contribution statement

J. Martín-de León: Writing – review & editing, Writing – original draft, Visualization, Validation, Methodology, Investigation, Formal

analysis, Data curation, Conceptualization. **J.L. Pura:** Writing – review & editing, Validation, Software, Investigation, Formal analysis, Conceptualization. **M.L. Rodríguez-Méndez:** Writing – review & editing, Validation, Funding acquisition. **M.A. Rodríguez-Pérez:** Writing – review & editing, Visualization, Validation, Supervision, Project administration, Funding acquisition.

Declaration of competing interest

The authors declare the following financial interests/personal relationships which may be considered as potential competing interests: Miguel Angel Rodriguez Perez reports financial support was provided by Spain Ministry of Science and Innovation. Miguel Angel Rodriguez Perez reports financial support was provided by Junta de Castilla y León Consejería de Educación. Miguel Angel Rodriguez Perez reports financial support was provided by EU Next Generation. If there are other authors, they declare that they have no known competing financial interests or personal relationships that could have appeared to influence the work reported in this paper.

Data availability

Data will be made available on request.

Acknowledgments

Financial support from the Science and Innovation Ministry of Spain (RTI2018-098749-B-I00 and PID2021-127108OB-I00, TED2021-130965B-I00 and PDC2022-133391-I00) is grateful acknowledged. Financial assistance from the Junta of Castille and Leon (VA202P20) is gratefully acknowledged. Activities funded by the EU NextGeneration and Castille and Leon. Complementary plans of research and development with the autonomous regions in actions of R&D. Component 17. Investment 1. (C17. I1), of the recovery, transformation and resilience plan.

Appendix A. Supplementary data

Supplementary data to this article can be found online at https://doi.org/10.1016/j.eurpolymj.2024.113181.

References

[1] T. Fujie, Development of free-standing polymer nanosheets for advanced medical and health-care applications, Polym. J. (2016) 773–780, https://doi.org/10.1038/pj.2016.38.
[2] K. Maex, M.R. Baklanov, D. Shamiryan, F. Iacopi, S.H. Brongersma, Z. S. Yanovitskaya, Low dielectric constant materials for microelectronics, J. Appl. Phys. 93 (11) (2003) 8793–8841, https://doi.org/10.1063/1.1567460.
[3] U. Okoroanyanwu, Thin film instabilities and implications for ultrathin resist processes, J. Vacuum Sci. Technol. B: Microelectron. Nanometer Struct. 18 (6) (2000) 3381, https://doi.org/10.1116/1.1321291.
[4] P.H. Pfromm, W.J. Koros, Accelerated physical ageing of thin glassy polymer films: evidence from gas transport measurements, Polymer (Guildf) 36 (12) (1995) 2379–2387, https://doi.org/10.1016/0032-3861(95)97336-E.
[5] C.J. Ellison, J.M. Torkelson, Sensing the glass transition in thin and ultrathin polymer films via fluorescence probes and labels, J. Polym. Sci. B Polym. Phys. 40 (24) (2002) 2745–2758, https://doi.org/10.1002/polb.10343.
[6] S.G. Isaacson, K. Lionti, W. Volksen, T.P. Magbitang, Y. Matsuda, R.H. Dauskardt, G. Dubois, Fundamental limits of material toughening in molecularly confined polymers, Nat. Mater. 15 (3) (2016) 294–298, https://doi.org/10.1038/nmat4475.
[7] Y. Grohens, L. Hamon, G. Reiter, A. Soldera, Y. Holl, Some relevant parameters affecting the glass transition of supported ultra-thin polymer films, Eur. Phys. J. E 8 (2) (2002) 217–224, https://doi.org/10.1140/epje/i2001-10088-4.
[8] C.B. Roth, Polymers under nanoconfinement: where are we now in understanding local property changes? Chem. Soc. Rev. 50 (14) (2021) 8050–8066, https://doi.org/10.1039/d1cs00054c.
[9] A.J. Crosby, J.Y. Lee, Polymer nanocomposites: the “nano” effect on mechanical properties, Polym. Rev. 47 (2) (2007) 217–229, https://doi.org/10.1080/15583720701271278.
[10] J.H. van Zanten, W.E. Wallace, W. Wu, Effect of strongly favorable substrate interactions on the thermal properties of ultrathin polymer films, Phys. Rev. E 53 (3) (1996) 2053–2056.
[11] M.A. Fanovich, P. Jaeger, Sorption and diffusion of compressed carbon dioxide in polycaprolactone for the development of porous scaffolds, Mater. Sci. Eng. C 32 (4) (2012) 961–968, https://doi.org/10.1016/j.msec.2012.02.021.
[12] J.A. Forrest, K. Dalnoki-Veress, J.R. Dutcher, Interface and chain confinement effects on the glass transition temperature of thin polymer films, Phys. Rev. E Stat. Phys. Plasmas Fluids Relat Interdiscip. Topics 56 (5) (1997) 5705–5716, https://doi.org/10.1103/PhysRevE.56.5705.
[13] C.A. Tweedie, G. Constantinides, K.E. Lehman, D.J. Brill, G.S. Blackman, K.J. Van Vliet, Enhanced stiffness of amorphous polymer surfaces under confinement of localized contact loads, Adv. Mater. 19 (18) (2007) 2540–2546, https://doi.org/10.1002/adma.200602846.
[14] C.J. Ellison, R.L. Ruszkowski, N.J. Fredin, J.M. Torkelson, Dramatic reduction of the effect of nanoconfinement on the glass transition of polymer films via addition of small-molecule diluent, Phys. Rev. Lett. 92 (9) (2004) 1–4, https://doi.org/10.1103/PhysRevLett.92.095702.
[15] C.M. Stafford, B.D. Vogt, C. Harrison, D. Julthongpiput, R. Huang, Elastic moduli of ultrathin amorphous polymer films, Macromolecules 39 (15) (2006) 5095–5099, https://doi.org/10.1021/ma060790i.
[16] P.M. Yiu, H. Yuan, Q. Gu, P. Gao, O.K.C. Tsui, Strain rate and thickness dependences of elastic modulus of free-standing polymer nanometer films, ACS Macro Lett. 9 (11) (2020) 1521–1526, https://doi.org/10.1021/acsmacrolett.0c00471.
[17] J.H. Zhao, M. Kiene, C. Hu, P.S. Ho, Thermal stress and glass transition of ultrathin polystyrene films, Appl. Phys. Lett. 77 (18) (2000) 2843–2845, https://doi.org/10.1063/1.1322049.
[18] J.M. Torres, C.M. Stafford, B.D. Vogt, Impact of molecular mass on the elastic modulus of thin polystyrene films, Polymer (Guildf) 51 (18) (2010) 4211–4217, https://doi.org/10.1016/j.polymer.2010.07.003.
[19] K. Yoshimoto, T.S. Jain, P.F. Nealey, J.J. De Pablo, Local dynamic mechanical properties in model free-standing polymer thin films, J. Chem. Phys. 122 (14) (2005), https://doi.org/10.1063/1.1873732.
[20] B.D. Vogt, Mechanical and viscoelastic properties of confined amorphous polymers, J. Polym. Sci. B Polym. Phys. 56 (1) (2018) 9–30, https://doi.org/10.1002/polb.24529.
[21] X. Cheng, K.W. Putz, C.D. Wood, L.C. Brinson, Characterization of local elastic modulus in confined polymer films via AFM indentation, Macromol. Rapid Commun. 36 (4) (2015) 391–397, https://doi.org/10.1002/marc.201400487.
[22] P.A. O’Connel, S.A. Hutcheson, G.B. McKenna, Creep behavior of ultra-thin polymer films, J. Polym. Sci. B Polym. Phys. 46 (2008) 1952–1965, https://doi.org/10.1002/polb.
[23] L. Li, L.M. Encarnacao, K.A. Brown, Polymer nanomechanics: separating the size effect from the substrate effect in nanoindentation, Appl. Phys. Lett. 110 (4) (2017), https://doi.org/10.1063/1.4975057.
[24] R.D. Priestley, D. Cangialosi, S. Napolitano, On the equivalence between the thermodynamic and dynamic measurements of the glass transition in confined polymers, J. Non Cryst. Solids 407 (2015) 288–295, https://doi.org/10.1016/j.jnoncrysol.2014.09.048.
[25] R.L. Jones, S.K. Kumar, D.L. Ho, R.M. Briber, T.P. Russell, Chain conformation in ultrathin polymer films using small-angle neutron scattering, Macromolecules 34 (3) (2001) 559–567, https://doi.org/10.1021/ma001141o.
[26] J.M. Rathfon, R.W. Cohn, A.J. Crosby, J.P. Rothstein, G.N. Tew, Confinement effects on chain entanglement in free-standing polystyrene ultrathin films, Macromolecules 44 (13) (2011) 5436–5442, https://doi.org/10.1021/ma1026324.
[27] R.K. Bay, S. Shimomura, Y. Liu, M. Ilton, A.J. Crosby, Confinement effect on strain localizations in glassy polymer films, Macromolecules 51 (10) (2018) 3647–3653, https://doi.org/10.1021/acs.macromol.8b00385.
[28] A. Gannepalli, D.G. Yablon, A.H. Tsou, R. Proksch, Erratum: Mapping nanoscale elasticity and dissipation using dual frequency contact resonance AFM (Nanotechnology (2011) 22 (355705)), Nanotechnology 24 (15) (2013), https://doi.org/10.1088/0957-4484/24/15/159501.
[29] R. Garcia, R. Proksch, Nanomechanical mapping of soft matter by bimodal force microscopy, Eur. Polym. J. 49 (8) (2013) 1897–1906, https://doi.org/10.1016/j.eurpolymj.2013.03.037.
[30] S. Benaglia, C.A. Amo, R. Garcia, Fast, Quantitative and high resolution mapping of viscoelastic properties with bimodal AFM, Nanoscale 11 (32) (2019) 15289–15297, https://doi.org/10.1039/c9nr04396a.
[31] H.K. Nguyen, M. Ito, K. Nakajima, Elastic and viscoelastic characterization of inhomogeneous polymers by bimodal atomic force microscopy, Jpn J. Appl. Phys. 55 (8) (2016), https://doi.org/10.7567/JJAP.55.08NB06.
[32] J. Martín-de León, M. Jiménez, J.L. Pura, V. Bernardo, M.A. Rodriguez-Pérez, Easy-way production of highly transparent nanocellular polymers films, Polymer (Guildf) (2021) 236, https://doi.org/10.1016/j.polymer.2021.124298.
[33] S. Costeux, S.P. Bunker, H.K. Jeon, Homogeneous nanocellular foams from styrenic-acrylic polymer blends, J. Mater. Res. 28 (17) (2013) 2351–2365, https://doi.org/10.1557/jmr.2013.100.
[34] J. Martín-de León, V. Bernardo, M.Á. Rodríguez-Pérez, Low density nanocellular polymers based on PMMA produced by gas dissolution foaming: fabrication and cellular structure characterization, Polymers (Basel) 8 (7) (2016) 265, https://doi.org/10.3390/polym8070265.
[35] J. Martín-De León, V. Bernardo, M.Á. Rodriguez-Perez, Cyclic gas dissolution foaming as an approach for simultaneously reducing cell size and relative density in nanocellular PMMA, Polymers (Basel) 13 (14) (2021), https://doi.org/10.3390/polym13142383.
[36] J. Martín-de León, J.L. Pura, V. Bernardo, M.Á. Rodríguez-Pérez, Transparent nanocellular PMMA: characterization and modeling of the optical properties,

Polymer (Guildf) 170 (March) (2019) 16–23, https://doi.org/10.1016/j.polymer.2019.03.010.
[37] R.G. Kirste, W.A. Kruse, K. Ibel, Determination of the conformation of polymers in the amorphous solid state and in concentrated solution by neutron diffraction, Polymer (Guildf) 16 (2) (1975) 120–124, https://doi.org/10.1016/0032-3861(75)90140-8.
[38] J. Martin-de Leon, F. Van Loock, V. Bernardo, N.A. Fleck, M.A. Rodriguez-Pérez, The influence of cell size on the mechanical properties of nanocellular PMMA, Polymer (Guildf) 181 (June) (2019) 121805, https://doi.org/10.1016/j.polymer.2019.121805.
[39] D. Miller, V. Kumar, Microcellular and nanocellular solid-state polyetherimide (PEI) foams using sub-critical carbon dioxide II. Tensile and impact properties, Polymer (Guildf) 52 (13) (2011) 2910–2919, https://doi.org/10.1016/j.polymer.2011.04.049.
[40] J. Pinto, E. Solorzano, M.A. Rodriguez-Perez, J.A. de Saja, Characterization of the cellular structure based on user-interactive image analysis procedures, J. Cellular Plast. 49 (7) (2013) 555–575, https://doi.org/10.1177/0021955X13503847.
[41] V. Kumar, N.P. Suh, A process for making microcellular thermoplastic parts, Polym. Eng. Sci. 30 (20) (1990) 1323–1329, https://doi.org/10.1002/pen.760302010.
[42] L.J. Gibson, M.F. Ashby, Cellular Solids: Structure and Properties, second ed., Cambridge University Press, United States, Cambridge, 1997.
[43] R. Proksch, D.G. Yablon, Loss tangent imaging: theory and simulations of repulsive-mode tapping atomic force microscopy, Appl. Phys. Lett. 100 (7) (2012) 073106, https://doi.org/10.1063/1.3675836.
[44] A. Labuda, M. Kocun, W. Meinhold, D. Walters, R. Proksch, Generalized hertz model for bimodal nanomechanical mapping, Beilstein J. Nanotechnol. 7 (1) (2016) 970–982, https://doi.org/10.3762/bjnano.7.89.